



- Large Eddy Simulation of the IEA 15-MW Wind Turbine Using a Two-Way Coupled Fluid-Structure Interaction Model
- Claudio Bernardi¹, Stefania Cherubini¹, Felice Manganelli¹, Giacomo Della Posta², Stefano Leonardi³, and Pietro De Palma¹
- ¹Department of Mechanics, Mathematics and Management, Polytechnic University of Bari, 70126, Bari, Italy (claudio.bernardi@poliba.it, stefania.cherubini@poliba.it,

f.manganelli@phd.poliba.it, pietro.depalma@poliba.it)

- ²Department of Mechanical and Aerospace Engineering, Sapienza University of Rome, Rome, RM, 00184, Italy (giacomo.dellaposta@uniroma1.it)
- Department of Mechanical Engineering, University of Texas at Dallas, Richardson, TX, 75080, USA (stefano.leonardi@utdallas.edu)
- 12 Correspondence: Claudio Bernardi (claudio.bernardi@poliba.it)

3 Abstract

The aim of the work is studying the aeroelastic response of the 15 MW NREL-IEA largescale wind turbine using a high-fidelity fluid-structure interaction solv large-eddy simulation with a modal computational structural dynamics solver through a two-way coupling. The fluid solver employs the actuator line model to simulate the 17 interaction between the turbine blades and the fluid and the immersed boundary method to model the presence of the tower and nacelle. The results are compared with those obtained by the OpenFAST software, which is a well-known numerical tool for engineering predictions. A series of simulations have been performed with and without the presence of the tower and nacelle to better understand the effects of these components on flow structures and structural deformations. The largest discrepancies among the solvers have been observed in correspondence with the blade passage in front of the tower, which induces an abrupt alteration in the local incidence angle of the flow. Moreover, by comparing the outcomes of different structural approximations, it has been established that taking into account the torsional degree of freedom considerably affects the deformations, aerodynamic loads and power coefficient. Whereas, the nonlinearity of the solver appears to have a weak effect on the same quantities.





30 Keywords

- 31 Aeroelasticity, Large Eddy Simulation, Actuator Line Model, Fluid-Structure Interaction, Computa-
- 22 tional Fluid Dynamics, Computational Structural Dynamics, Blade Element Momentum, IEA-15MW
- Wind Turbine.

1 Introduction

Wind energy has become a crucial component of the global transition toward renewable energy sources. The increasing demand for clean energy has led to the development of large-scale wind turbines, such as the IEA 15-MW offshore wind turbine developed within IEA Wind Task 37 (Gaertner et al., 2020). This turbine, with a rotor diameter of 240 meters and blades measuring 117 meters in length, rep-38 resents a new frontier in wind energy technology (Gaertner et al., 2020), and research is currently 39 pointing towards even larger rotors, reaching 22-MW of power production (Zahle et al., 2024). The 40 increasing scale and flexibility of such newly designed turbines present significant engineering chal-41 lenges, particularly in predicting their aeroelastic response (Burton et al., 2011; Zheng et al., 2023). 42 As turbines grow in size, their structural components, especially the blades, are subject to complex aerodynamic forces that cause deformations, which in turn affect the aerodynamic loads. Understand-44 ing these interactions is essential to improve the performance, reliability, and longevity of large-scale wind turbines (Manwell et al., 2010). In the worst cases, aeroelastic instabilities such as edgewise instability and flutter might even lead to blade damage, as reported for the Lunderskov Mobelfabrik 47 19 m wind turbine blades (Moeller, 1997), with devastating effects on the turbine performance. dy of the interaction between aerodynamic, inertial and elastic forces due to the Aeroelasticity, the 49 deformation of t cuture, is critical in the design and analysis of modern wind turbines. Aeroe-50 lastic phenomena such as dynamic stall, flutter, and | can have significant effects on turbine 51 performance, particularly as the blade length increases (mansen, 2007). These blades experience vary-52 ing aerodynamic forces along their span, which can lead to substantial deformations. When blades deform, they alter the local flow field, which in turn modifies the aerodynamic loads acting on them. 54 This feedback loop between aerodynamic forces and structural deformation makes it very difficult 55 to predict modern large-scale turbine performance under real-world operating conditions (Vermeer et al., 2003; Wang et al., 2016). Accurate evaluation of these interactions is key for ensuring turbine 57 efficiency and structural integrity, especially in offshore environments where wind conditions are more severe (Bayati et al., 2017). The numerical modeling of the blades in most of the numerical aeroelastic codes used nowadays (Schepers et al., 2021) is accomplished by the blade element multiple turn (BEM) model, due to its robustness 60 tum (BEM) model, due to its robustness 61 and low computational cost. However, BEM has several limitations, due to the strong assumptions 62 made on the impinging flow, requir delta of dynamic stall, dynamic inflow, yaw and tilt flows, and corrections of the aerofoil data tracking into account three-dimensional effects and tip losses. Unfortunately, more computationally expensive models, such as the free-wake panel and the actuator disc m s, are not able to predict the dynamic loading much more accurately. Therefore, the 66 application of computational fluid dynamics (CFD) to full-scale turbines is the most promising way to drop those assumptions and describe the complex aerodynamics of the flow field more accurately





(Sørensen, 2011). However, coupling three-dimensional CFD simulations with computational structural dynamics (CSD) solvers taking into account the deformation of the blade is not trivial. Three-dimensional structural finite-element models are in fact able to fully describe the complex shape of a wind turbine blade but, 72 although accurate, these models are computationally expensive and hard to implement, leading to 73 only a few examples of coupling with CFD codes (Bazilevs et al., 2011; Yu and Kwon, 2014). Since 74 wind turbine blades are slender structures, their structural modeling can be more easily achieved using 75 beam models, where the blade is approximated as a series of one-dimensional beam elements, each characterised by a given cross-section iffness and mass per unit length. One-dimensional beam models can be either modal, since natural frequencies and mode shapes of a turbine are directly re-78 lated to the natural frequencies of its blades, or they can rely on the geometrically exact beam theory 79 including non-linear effects (Sabale and Gopal, 2019). 80 Due to their ability to provide a rapid evaluation of the turbine performance, numerical tools based on the lifting-line approach equal with aeroelastic modules based on one-dimensional beam models, are currently widespread (Sex-pers et al., 2021). A notable example is OpenFAST, a numerical code 83 developed at NREL (Jonkman, Jonkman) and widely used for aeroelastic simulations, which employs 84 BEM theory for aerodynamic modeling and various structural solvers, such as ElastoDyn (Damiani 85 et al., 2015) and BeamDyn (Wang et al., 2016), for structural deformation analysis. However, it is still not clear whether the predictions of such lifting aeroelastic codes are sufficiently accurate for large-scale turbines, in which the effect of shear and we turbulence can lead to complex inflows and turbine aerodynamic responses. Comparing the predictions of OpenFAST with those of a Large-Eddy Simulation (LES) equipped with a structural one-dimensional beam model has shown that, for an 90 NREL 5MW wind turbine, the passage in front of the tower leads to large deformations which are 91 largely underestimated by OpenFAST (Bernardi et al., 2023). 92 Concerning rotors of even larger size, such as the IEA 15-MW reference turbine, it is not yet known whether these discrepancies in the predictions of lifting codes with respect to CFD are even more consistent. Using the unsteady Reynolds-Average vier-Stokes (URANS) equations coupled with 95 an aeroelastic module, as reported by Pagamonci et al. (2023), has shown that neglecting the flexibility 96 of the blades in numerical simulations leads to an underestimation of the rotor thrust of approximately 97 2.5% for the IEA 15-MW turbine, which is not observed for the smaller NREL 5MW rotor. Moreover, this work also concluded that the deformation of long, slender blades may act as a filter for the high-frequency fluctuations arising from the flow field, proving that taking into account the blades' 100 aeroelasticity in the design process of these machines is key for the future upscaling of turbine rotors. 101 Furthermore, Trigaux et al. (2024) observed how the use of high-fidelity aerodynamic models is crucial 102 to predict the aeroelastic effects of large rotors. These results suggest the need to investigate this issue 103 resorting to LES, which is capable of describing the dynamics of the flow more accurately. 104 In this context, the present work aims at studying the aeroelastic response of a large-scale 15-MW 105 wind turbine by means of LES, assessing the effect of the flexibility of the blades on the wake dynam-106 ics. The results are compared with those obtained by more simple and less computationally expensive 107 models, such as the OpenFAST code. Computations are performed by an in-house LES code using 108 the immersed boundary method to model the tower and nacelle and the Actuator Line Model (ALM)

for blade modeling, coupled with a structural modal solver, originally developed by Della Posta et al.





(2022).111

119

The discussion of the results highlights the role of the tower and nacelle in the dynamics of the aerodynamical forces, thrust and power coefficients, as well as in the distribution of turbulent kinetic energy 113 within the wake, which could have an impact on the aerodynamic loads of downstream turbines in 114 wind farms. Moreover, the effect of the torsional degree of freedom has been investigated by comparing 115 the outcomes of different structural approximations. 116 The work is structured as follows. In section 2, the aerodynamic and structural solvers of both CFD-117 CSD and OpenFAST codes are described in detail. In section 3, the numerical setup is presented. In section 4, relevant results are discussed, and conclusions are drawn in section 5.

$\mathbf{2}$ Methodologies 120

2.1CFD-CSD solver 121

2.1.1 Flow solver 122

The simulations of the flow around the wind turbine are carried out through Large-Eddy Simulations (LESs) of the incompressible, filtered, 3D Navier-Stokes equations, employing our in-house UTD-WF 124 solver (Santoni et al., 2020). The code implements a second-order accurate cent finite difference 125 scheme for the spatial discretization on a staggered Cartesian grid. A hybrid low-vorage third-order-126 accurate Runge-Kutta (RK) scheme is used for time integration of the non-linear terms (Orlandi, 127 2012), while the linear terms are treated implicitly using a Crank-Nicolson scheme. The filtered governing equations are:

$$\frac{\partial u_i}{\partial t} + \frac{\partial u_i u_j}{\partial x_j} = -\frac{\partial p}{\partial x_i} + \frac{1}{Re} \frac{\partial^2 u_i}{\partial x_j \partial x_j} - \frac{\partial \tau_{ij}}{\partial x_j} + \tilde{f}_i, \tag{1}$$

$$\frac{\partial u_i}{\partial x_i} = 0, \tag{2}$$

$$\frac{\partial u_i}{\partial x_i} = 0,$$
 (2)

where $i, j \in \{1, 2, 3\}$ represent, in a Cartesian reference frame, the components along the stream-130 wise, wall-normal, and spanwise directions, respectively. The Reynolds number $Re = U_{\infty}D/\nu$ is 131 defined by the undisturbed inlet velocity U_{∞} , the turbine diameter D, and the kinematic viscosity of 132 the fluid ν . These quantities are used as reference values to make the equations non-dimensional. To 133 134 solve the filtered equations, a Subgrid-Scale (SGS) stress model is needed. The latter describes the interaction between the large resolved and the sub-grid unresolved scales, as described by Pino Martín 135 et al. (2000) and Santoni et al. (2017). Here, we employ the Smagorinsky model with constant 136 $C_s = 0.09$ as discussed by Martinez-Tossas et al. (2018). 137 The effect of the blades on the flow is modeled by the Actuator Line Model (ALM) (Troldborg, 2009), 138 by adding a forcing term to the Navier-Stokes equations, representing the force per unit volume exerted by the rotor on the fluid. By approximating the rotor blades as rigid straight lines discretized 140 into segments, it is possible to estimate the lift and drag forces per unit ler _____ on a 2D plane as 141 follows: 142



147

148

149

150

151

167



$$F_l = \frac{1}{2}\rho u_{rel}^2 C_l(\alpha) cF, \qquad F_d = \frac{1}{2}\rho u_{rel}^2 C_d(\alpha) cF, \tag{3}$$

where ρ is the air density, c is the local chord, u_{rel} is the relative incoming velocity, α is the angle of attack, and F represents the Prandtl tip loss correction factor (Sh al., 2005). The forces are then projected on the flow employing a 2D Gaussian kernel, which spreads the lift and drag force vector, f^{aero} , in cylinders surrounding the actuator line,

$$\tilde{\mathbf{f}} = -\mathbf{f}^{aero} \frac{1}{\epsilon^2 \pi} exp \left[-\left(\frac{r_{\eta}}{\epsilon}\right)^2 \right],\tag{4}$$

where r_{η} is the radial distance of a generic point of the cylinder from the actuator line and ϵ is the spreading parameter, where $\epsilon/\Delta \geq 2$, with $\Delta = \sqrt{\Delta x^2 + \Delta y^2 + \Delta z^2}$, following Troldborg (2009). The tower and nacelle are modeled using the Immersed Boundary Method (IBM) following the approach described by Orlandi and Leonardi (2006).

From an aerodynamic standpoint, the rotor blades represent the most flexible components within a

2.1.2 Structural solver

153 wind turbine. Several studies demonstrated that their modal properties have a significant impact on the dynamics of the entire structure (Damgaard et al., 2013; Dong et al., 2018). Moreover, an analysis 154 of the isolated blades is also sufficient to accurately estimate the aeroelastic properties of the entire 155 structure, including the flutter speed (Abdel Hafeez and El-Badawy, 2018). Additionally, the tower 156 and shaft exhibit minimal deflection due to their stiffness. In light of the above considerations, the 157 aeroelastic model is constructed to encompass solely the structure of the blades. The structural model used in the present study was previously presented by Della Posta et al. (2022, 159 2023). In order to model the working conditions, the blades are assumed to be rotating beams rigidly 160 clamped at the hub (cantilever beams), under the assumption of small deformations we espect 161 to a relative frame of reference (FOR). The direction of the pitching axis is denoted by coincides with the neutral axis of the blade, defined as passing through the quarter of the chord. The direction of the out-of-plane flapwise motion is indicated by X_2 and is oriented in the positive 164 streamwise direction. The in-plane edgewise direction of X_3 is defined such that the FOR is oriented 165 as a right-handed coordinate system (Figure 1). 166

Under the assumption of linearity, the elastic generalised displacement d, which includes translational d_i and rotational θ_i degrees of freedom (DoFs), is decomposed along the coordinate X_1 on the neutral axis as:

$$\mathbf{d}(X_{1},t) = \sum_{m=1}^{M} q_{m}(t) \, \boldsymbol{\psi}^{m}(X_{1}), \qquad (5)$$

where $\psi^m(X_1)$ is the m-th elastic mode shape from the modal analysis of the structure, q_m is the corresponding modal coordinate, and M is the number of modes used. The general inertial coupling is included in a modal basis by means of the methodology introduced by Reschke (2005) and further developed for the case of wind energy by Della Posta et al. (2022). In particular, the two-way coupling



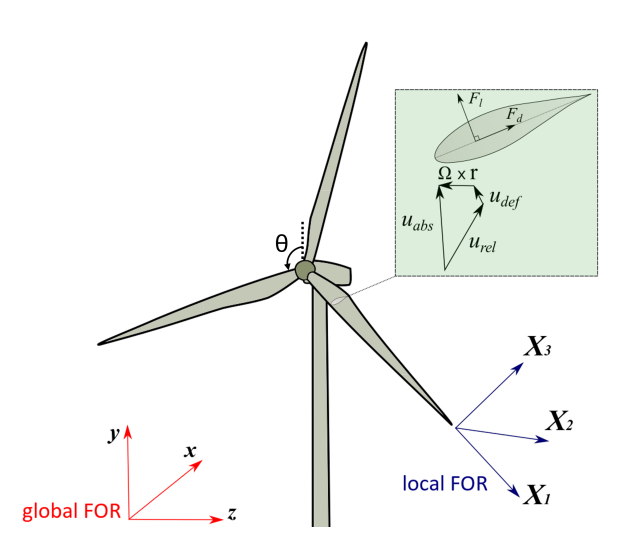


Figure 1: Sketch of the frames of reference used for the CFD and for the CSD simulations.

algorithm between rigid-body and structural dynamics does not take into account a modification of the rotor inertia caused by the deformation of the blades. e, the structural dynamics of the structure can be described by the following equation:

$$M\ddot{q} + [D + D^{Co}(\Omega)]\dot{q} + [K + K^{c}(\Omega) + K^{Eu}(\dot{\Omega})]q = e + e^{c}(\Omega) + e^{Eu}(\dot{\Omega}),$$
(6)

where M, D and K denote the modal structural mass, damping, and stiffness matrices, respectively, and e are the external loads expressed in modal basis. The remaining terms are inherently related to the various contributions to the acceleration in a moving FOR. Terms with the superscript Co, c and Eu are related to the Coriolis, centrifugal, and Euler accelerations, respectively. The discrete evaluation of the additional inertial terms in Equation (6) is expressed as a function only of the information known from the structural finite-element method (FEM) model at model and matrices are a finite element model of the blade based on complete beam elements with 6 Dometric Euler-Bernoulli behavior for bending in directions X_2 and X_3 , and linear shape functions for advance the structural dynamic equation in time, which is unconditionally stable for linear problems, and second-order ate. We assume a lumped-mass representation, and we take into account the local offset of the considering the local twist. Details about the modal analysis are provided in Appendix A.





2.1.3 Fluid-Structure Interaction model

The two-way coupling aeroelastic model employs the ALM sectional approach, whereby the angle of attack (AoA) and relative velocity are locally modified following the instantaneous blade motion provided by the structural dynamics. In particular, the distribution of the AoA along each blade is evaluated as a function of the velocity of the fluid, the angular velocity of the rotor, and the instantaneous elastic state of the blade. The latter is generally constructed from the deformation velocity $u_{def} = d$ and the local vector of the deformation angles θ (torsion and length length) derived from the structura er, which is forced by the updated aerodynamic loads. The algorithm restricts inter-field communications solely at the beginning of each RK substep, thereby ensuring optimal comp = bnal efficiency. The impact of torsional dynamics was deemed to be limited in light of the result soptained in previous studies on the effect of torsion for smaller wind turbines (Chen, 2017). In order to investigate this issue for the large rotor 15MW wind turbine, in this study we compare two different CSD models. In particular, we consider as a baseline a two-way coupling that includes the effect of blade deformation velocity as a sole variable (CFD-CSD/OV, for Only Velocity), and a more complete model including the torsional deformation in the coupling (CFD-CSD/T, for Torsional). In general, the relative velocity for a rotating blade can be defined with the following expression:

$$u_{rel} = u_{abs} - \Omega \times r_{OP} - u_{def}, \tag{7}$$

where u_{abs} is the filte elocity from the fluid solver at the actuator line, r_{OP} is the general radial vector pointing to the converged section, Ω is the rotor rotational speed, and u_{def} is the deformation velocity of the structure at the same position. As a result, the AoA used to determine the air load coefficients is defined as follows:

$$\alpha = \operatorname{atan}\left(\frac{\boldsymbol{u}_{rel} \cdot \boldsymbol{E}_2}{-\boldsymbol{u}_{rel} \cdot \boldsymbol{E}_3}\right) - \phi - \frac{\theta_{tors}}{-\theta_{tors}} = \operatorname{atan}\left[\frac{(\boldsymbol{u}_{abs} - \boldsymbol{u}_{def}) \cdot \boldsymbol{E}_2}{\Omega r - (\boldsymbol{u}_{abs} - \boldsymbol{u}_{def}) \cdot \boldsymbol{E}_3}\right] - \phi - \theta_{tors}, \tag{8}$$
where ϕ is the local twist angle of the $\boldsymbol{\psi}$, θ_{tors} is the local torsional deformation, \boldsymbol{E}_i are the

where ϕ is the local twist angle of the v_{total} , θ_{tors} is the local torsional deformation, E_i are the unit vectors of the relative FOR rotating with the structure, and hence, $v_2 = u_{def} \cdot E_2$ is the flapwise deformation velocity component, and $v_3 = u_{def} \cdot E_3$ is the edgewise deformation velocity component. The simplified coupling procedure benefits from the sectional one-dimensional formulation of the ALM, which avoids the complex treatment of the fluid-solid interface with the associated kinematic and traction conditions.

2.2 OpenFAST modules

For comparison putes, wind turbine simulations have been also conducted using the OpenFAST solver Release v3.2.0 (July 29, 2022). OpenFAST is a widely utilized open-source numerical code developed by the NREL that combines different specialized modules for simulating the coupled aero-hydro-servo-elastic response of wind turbines. The aerodynamic computations are performed by the AeroDyn (Jonkman et al., 2015) module which is based on the BEM theory. A Prandtl loss model is applied to account for the tip and root effects. The structural module dedicated to the computation of the blade deformation is contained in the BeamDyn module, which relies on the geometrically exact beam theory and may resolve geometric non-linearities and large deflections (Wang et al., 2016).





BeamDyn has replaced the simplified ElastoDyn module, based on a modal approach and suitable for blade deformation dominated by bending. In order to compare the CFD-CSD results with a modal structural analysis, we also performed simulations using the standalone ElastoDyn module. It is worth to notice that the latter does not take into account the torsional degree of freedom, so it is to be directly compared to the CFD-CSD/OV model, which also does not account for the coupling between the torsional deformation and the angle of attack. As reported in the original manual of AeroDyn (Moriarty and Hansen, 2005), OpenFAST couples the fluid and structural solvers in a similar way to our CFD-CSD solvers. In particular, the local angle of attack is determined taking into account the local deformation velocities.

235 3 Flow and structural setup

blades given by N=80 equally-spaced nodes were chosen.

In this work, we consider a stand-alone IEA 15-MW wind turbine (Gaertner et al., 2020) in its 236 monopile configuration. This wind turbine has a rotor diameter D=240 m with three blades of 237 length L=117 m. Table 1 provides the main features of the turbine. 238 The computational box has dimensions $12.5 \times 5 \times 3$ diameter units, as shown in Figure 2. More-239 over, following the content of the Appendix A, the computational box has been discretized by a stagger of grid composed of $2049 \times 513 \times 513$ points in the streamwise, wall-normal, 240 241 and spanwise directions, respectively. The orthogonal grid is equally spaced in the streamwise and 242 spanwise directions and is stretched vertically, with a gradually wider spacing starting from the region 243 above the rotor. The grid spacing described leads to an actuator line discretized by 86 points per 244 blade. The time resolution of the LES computation is tied to the spatial resolution, as defined by 245 the stability requirements of the numerical scheme adopted. Simulations are carried out at a constant 246 Courant–Friedrichs–Lewy (CFL) number (Courant et al., 1967) CFL = 0.65, which ensures an aver-247 age time step $\overline{\Delta t} = 0.024s$. The turbine location is 4 diameter units from the inlet and centered in 248 the spanwise direction. Furthermore, we impose a she laminar inflow velocity profile, defined by a 249 power law with the exponent $\alpha = 0.05$, and a radiative power law with the exponent $\alpha = 0.05$, and a radiative power law with the exponent $\alpha = 0.05$, and a radiative power law with the exponent $\alpha = 0.05$, and a radiative power law with the exponent $\alpha = 0.05$, and a radiative power law with the exponent $\alpha = 0.05$, and a radiative power law with the exponent $\alpha = 0.05$, and a radiative power law with the exponent $\alpha = 0.05$, and a radiative power law with the exponent $\alpha = 0.05$, and a radiative power law with the exponent $\alpha = 0.05$, and a radiative power law with the exponent $\alpha = 0.05$, and a radiative power law with the exponent $\alpha = 0.05$, and a radiative power law with the exponent $\alpha = 0.05$, and a radiative power law with the exponent $\alpha = 0.05$, and $\alpha = 0.05$ 250 rection, periodic boundary conditions are imposed. Moreover, slip and no-slip conditions are enforced 251 at the top and bottom boundaries, respectively. The turbine is subjected to a flow with a Reynolds 252 number $Re \approx 10^8$ and operates at its nominal tip speed ratio (TSR) of $\lambda = 9$. The streamwise 253 undisturbed velocity at the hub height is constant and equal to $U_{\infty} = 10 \ m/s$. The simulations were 254 conducted for a time interval of 300 s over the initial transient, which corresponds to 35 revolutions 255 of the rotor. To identify the optimal configuration for the structural model, we conducted a preliminary sensitivity analysis and then validated the structural eigenfre cies with the results found in the literature. A 258 more detailed insight into this analysis is presented in Appendix B, where the structural properties 259 of this turbine are shown. Finally, a number of modes $M_s = 15$ and a structural discretization of the 260





Parameter	Units	Value	
Power rating	MW	15	
Rotor diameter (D)	m	240	
Rotor orientation	_	Upwind	
Number of blades	_	3	
Blade length (L)	m	117	
Hub height	m	150	
Hub radius (R_{hub})	m	3.97	
Rated wind speed	m/s	10.59	
Design tip speed ratio	_	9	
Maximum rotor speed	RPM	7.56	

Table 1: IEA 15-MW (Gaertner et al., 2020) wind turbine main features

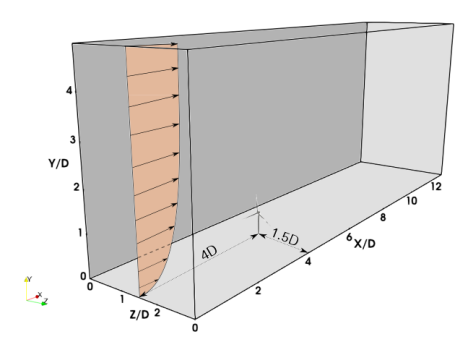


Figure 2: Sketch of the computational box where the incoming sheared flow and the position of the turbine are highlighted.

262 4 Results and Discussion

263

264

265

267

268

269

This section presents the results of two set of simulations: one modeling a rotor-only configuration (RO) and the other including the tower and nacelle (TN). Furthermore, both configurations are subjected to comparative analysis using the OpenFAST submodules. Firstly, the near-wake aerodynamic characteristics and the wake recovery of both configurations determined by the CFD-CSD solvers are discussed. Then, the aerodynamic loads on the blades are analyzed and the outcomes from both solvers are compared. Finally, the overall turbine performance and the effects on the blade deformation are assessed.



272

273

274

275

278

279

280

281

282

283

284

285

286

291

292

293



4.1 Flow analysis

As a first step, we analyze the flow field variables, as obtained using the CFD-CSD/T solver. Figure 3 illustrates the main coherent flow structures in the field by means of an instantaneous isosurface of the Q-criterion colored by the streamwise velocity for both cases. It is evident that the presence of the tower affects the vorticity intensity distribution along the vertical direction. In particular, the occurrence of a low-velocity recirculation zone at the tower height for the TN case can be identified, which is a result of the tower shadowing (see Figure 3b). Moreover, the TN case demonstrates a more rapid dissolution of the endogenous coherent hub vortex structures if compared to the RO case (see Figure 3a). On the other hand, the tip vortex structures appear to be minimally influenced by the presence of the tower. Figure 4 shows the rotor-averaged streamwise velocity along the flow direction, time-averaged over 30 revolutions of the rotor. Contrary to what Santoni et al. (2017) observed in their work on the 5MW reference turbine invested by a uniform inflow, the rotor-averaged velocity for the TN configuration in the wake remains slightly lower than for the OR case, indicating that wake recovery is slightly hindered by the presence of the tower. The reason for this behavior can be found in the different aspect ratio of the tower for the present turbine. In particular, for the NREL 5-MW turbine, the ratio between the tower diameter and the rotor diameter is about equal to 0.047, whereas, for the 15MW turbine, it is only about 0.027 (the tower diameters being 6m and 6.5m, respectively). Thus, the thinner shape (in terms of diameter units) of the tower, as well as the lower value of the incoming velocity at the tower height due to the presence of shear at the inflow, result into a decreased mixing behind the turbine which leads to a slower wake recovery.

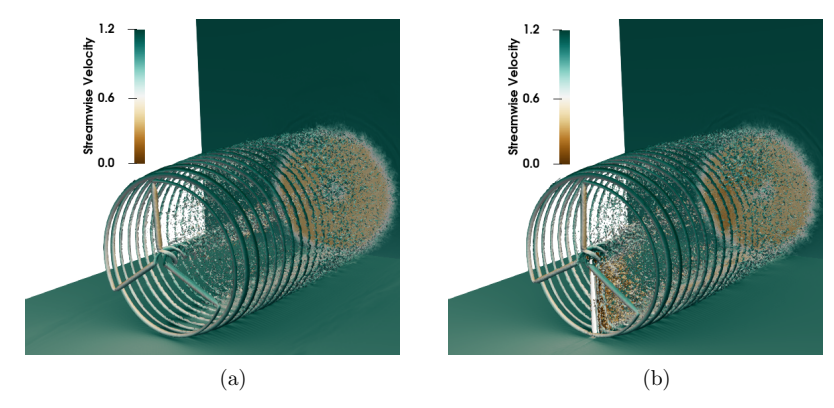


Figure 3: Q-criterion contour of the instantaneous velocity field colored by the streamwise velocity for the rotor-only case (RO) (a) and tower and nacelle (TN) (b).

From an energy perspective, the wake recovery process can be depicted by examining the Turbulent Kinetic Energy (TKE) in the wake. Figure 5 represents the time-averaged TKE for both configurations on different planes. The TN case exhibits high TKE values in the near wake, in the region just downstream of the tower and nacelle. The top view of the TN case shows that the TKE in the wake presents an asymmetric distribution as De Cillis et al. (2022) observed, among the others, in their



296

297

298

300

301

302

303

305

306

307

308

309

310

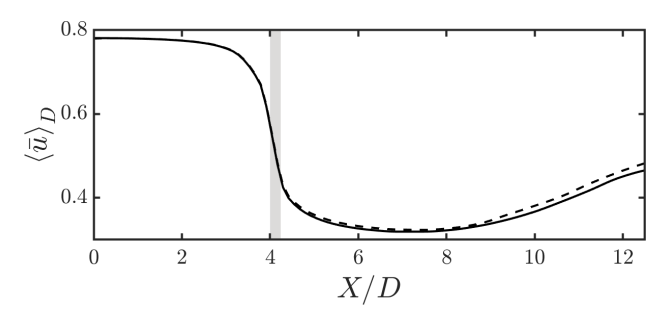


Figure 4: Rotor-averaged velocity along the streamwise direction normalized by the undisturbed velocity at the rotor height, namely, $U_{\infty} = 10 \ m/s$. The grey region represents the area covered by the rotor. (RO ----, TN ——).

work. On the contrary, the RO configuration shows large TKE only in the far wake region, with large values also in the region above hub height. This suggests that the tower does not increase the kinetic energy entrainment but it rather has a slight shielding effect on wake recovery. Although not favoring kinetic energy entrainment, the tower still plays a strong role in the wake dynamics, as it can be visualized in figure 6, showing slices of instantaneous streamwise velocity at different tower heights corresponding to 80% of the blade (top) and to the tip of the blade (bottom), when the blade is in front of the tower, i.e. $\theta = 180^{\circ}$ (left), and when it is far from it (right). In particular, it can be observed that the turbulent mixing right downstream of the tower is already very high in the near wake compared to that close to the tip of the blades. Probably due to asymmetry induced by the rotation of the blades, inside the rotor disk, it can be seen that the tower wake bends in the spanwise direction (Figure 6, top frames), whereas it is rather spanwise independent at a height corresponding to the blade's tip (bottom frames). Moreover, one can see that the passage of the blade in front of the tower (left frames) induces a strong perturbation in the flow field already upstream of the tower. In the following section, the effect of this perturbation on the phase oscillations of several relevant quantities (aerodynamic forces, power coefficient, etc.) will be discussed.

4.2 Aerodynamic loads on the blade

The analysis of the aerodynamic loads on the blade has been conducted using the present CFD-CSD 311 models and the engineering software OpenFAST. The same laminar sheared inflow is imposed for both 312 solvers using a power law with the same exponent and reference streamwise velocity at the hub height. 313 We have chosen not to impose a turbulent inflow to avoid differences in the definition of the turbulent 314 inflow itself which might have hindered the comparison between the results of the two codes. 315 Figure 7 depicts the following time-averaged aerodynamic quantities along the span of the blade: the 316 local angle of attack α (Figure 7a); the aerodynamic pitching moment per unit length M_{aero} (Figure 317 7b); the flapwise and edgewise components o aerodynamic force per unit length F_2 (Figure 7c) 318 and F_3 (Figure 7d), respectively. In particular, Figure 7a shows that a goo eement of the local 319



321

324

325

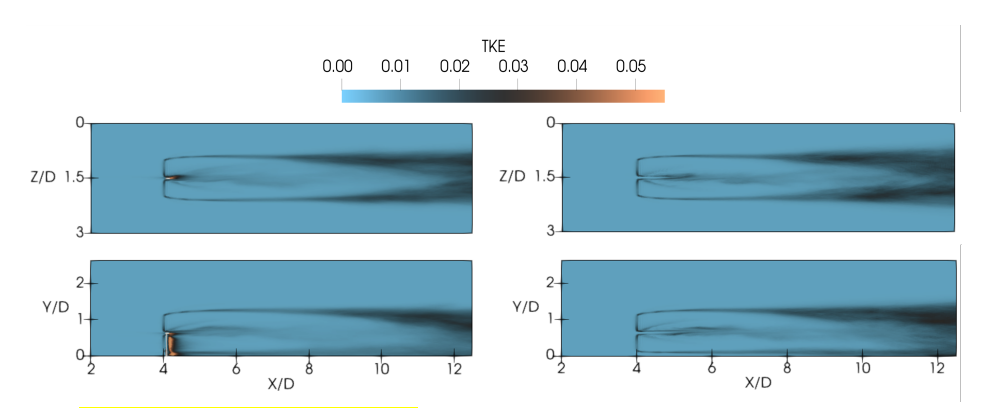


Figure 5: Top (upper slices) and lateral (lower slices) views of the time-averaged Turbulent Kinetic Energy on slices passing through the hub. TN (left), RO (right).

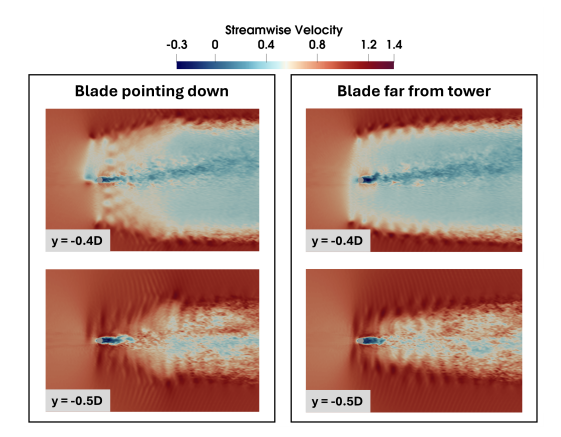


Figure 6: Instantaneous streamwise velocity on horizontal slices at different tower heights corresponding to 80° he blade (top slices), and the tip of the blade (bottom slices). In the left configuration, the blade is in front of the tower ($\theta = 180^{\circ}$), while on the right the blade is far from the tower.

incidence angle computed by both CFD-CSD models (solid lines) with that computed by ElastoDyn (circles) and BeamDyn (squares) is obtained from the 20% up to the 80% of the blade length. Indeed, the differences in the root area are ascribable to the presence of the hub which is modeled differently by the solvers. The discrepancy of the incidence angle observed towards the tip subsequently affects the aerodynamic loads. The F_2 force in Figure 7c shows a very good fit of the CFD-CSD/T results with that of the nonlinear solver BeamDyn, despite the linearity of our in-house CSD model. The strong discrepancies with respect to the values obtained by ElastoDyn can be ascribed to the absence





of the torsional deformation in the latter solver. Indeed, the CFD-CDS/OV solver, which neglects the torsional feedback in the coupling, shows very similar results to the ElastoDyn solver. A similar effect can be observed by examining the reduction in F_3 towards the tip of the blade (see Figure 7d). The distribution of the aerodynamic pitching moment presents instead a maximum gap of about 8% from the BEM-based solvers.

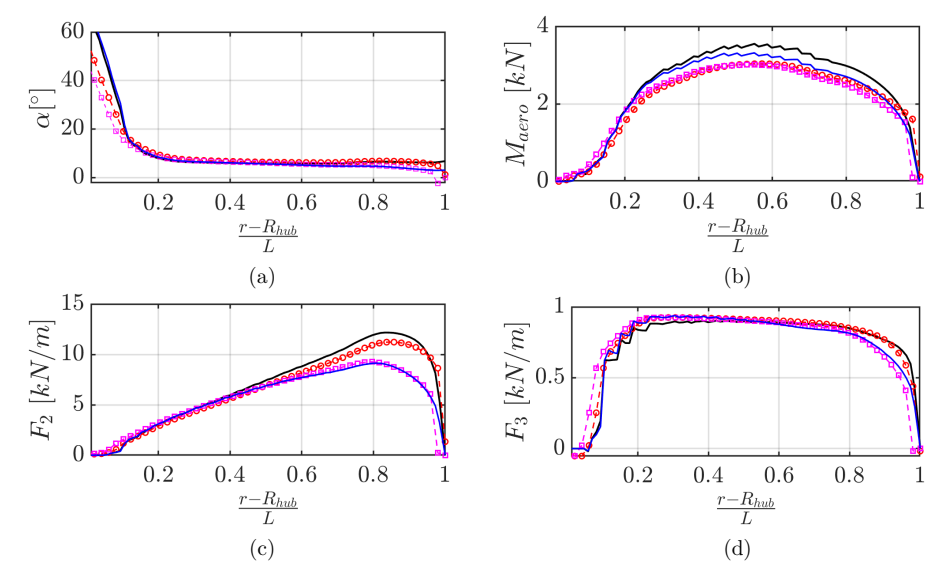


Figure 7: Average aerodynamic quantities along the blade compared between CFD-CSD/OV (black solid line), CFD-CSD/T (blue solid line), ElastoDyn (red rounded markers), BeamDyn (magenta squared markers). (a) ence angle, (b) Aerodynamic pitch moment, (c) flapwise aerodynamic force, (d) edgewise aerodynamic force.

As demonstrated by Hansen (2015), the outer third of the blade span is the most critical region in terms of deflections and deformations due to the combination of higher aerodynamic loads and reduced structural stiffness. Therefore, a phase average of the aerodynamic quantities at the 80% of the blade has been performed. Figure 8 reports the evolution of the incidence angle and of the aerodynamic force components at $\frac{r-R_{hub}}{L}=0.8$ (being R_{hub} the hub radius and L the blade length) versus the blade rotation angle θ . The dynamical behavior of the aerodynamic quantities in the presence (solid lines) or in the absence (dashed lines) of the tower underlines that the passage of the blade in front of the tower represents the main source of instability for the flow conditions considered. Indeed, the blade-tower interaction leads to an oscillations of the aerodynamic forces and of the incidence angle around $\theta=180^{\circ}$, i.e., when the blade is pointing down. However, unlike the case of the NREL 5-MW turbine (Bernardi et al., 2023), this effect appears to be stronger for the BEM computations than for the CFD-CSD solver. Concerning this point, we should recall that, as pointed out by Bernardi



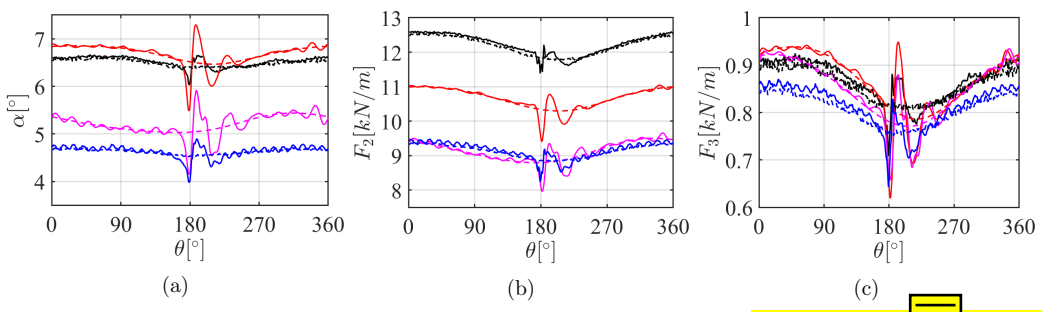


Figure 8: Phase-averaged values of: (a) the local incidence angle, (b) flapwise aerody angential aerodynamic force at the 80% of the blade. CFD-CSD/OV: TN -CFDCSD/T: TN —, RO ----. ElastoDyn: TN —, RO ----. BeamDyn: TN —

et al. (2023), the complex flow dynamics resulting from the interaction between the blade and the tower, shown in Figure 6, may not be well described by OpenFAST, which uses a simple potential 345 flow model. It can be observed that, between the rotor and the tower, a region with low streamwise 346 velocity is observed. We can expect that the passage of the blade in front of the tower thus induces 347 an alteration of the aerodynamic forces on the blade due to the decrease/increase of the streamwise 348 velocity. This issue will be further discussed in the following, where a possible reason for the different 349 behavior observed for the IEA 15-MW with respect to the NREL 5-MW turbine will be discussed. 350 Apart from the effect of the tower, one can observe a rather good match between the CFD-CSD/OV 351 and ElastoDyn solvers for both the incidence angle and the edgewise component of the aerodynamic 352 353 force, while the flapwise component presents some discrepancies. On the other hand, when torsional feedback is included, CFD-CSD/T and BeamDyn solvers agree rather well for all the quantities con-354 sidered, regardless of the linearity or non-linearity of the models. 355 To better investigate the local response of the different models during the blade revolution, we con-356 ducted a comparative analysis of the aerodynamic loads, employing phase-averaged quantities over 357 the span. Figure 9 illustrates the percentage difference of the phase-averaged aerodynamic quantities on the rotor plane of the ElastoDyn (BeamDyn) solver with respect to the CFD-CSD/OV (CFD-359 CSD/T) model, respectively. In particular, in comparison to ElastoDyn, a higher value of the absolute 360 incidence angle in the range of $\Delta \alpha / \alpha^{CFD-CSD/OV}$ | = [17%, 25%] is found in the zone after the tower (see Figure 9a). The difference we spect to the results obtained by BeamDyn tends to be higher moving from the root to the tip with a discontinuity in the tower area, spanning the range 361 362 363 $|\langle \Delta \alpha / \alpha^{CFD} \rangle^{\%}| = [35\%, 60\%]$ in the last 20% of the blade span. Furthermore, the angle of attack 364 distribution affects the components of the aerodynamic force. In fact, the distribution of the flapwise 365 component of the force follows the same pattern of the incidence angle (see Figure 9b). On the other 366 hand, for the edgewise component the major discrepancies are concentrated in the final radial sections 367 of the blade toward the tip (see Figure 9c). In general, we can conclude that the most significant 368 discrepancies are observed in the tip region where the three-dimensional effects are more relevant and 369 where the complexity of the fluid flow is strongly affected by the presence of the tower.



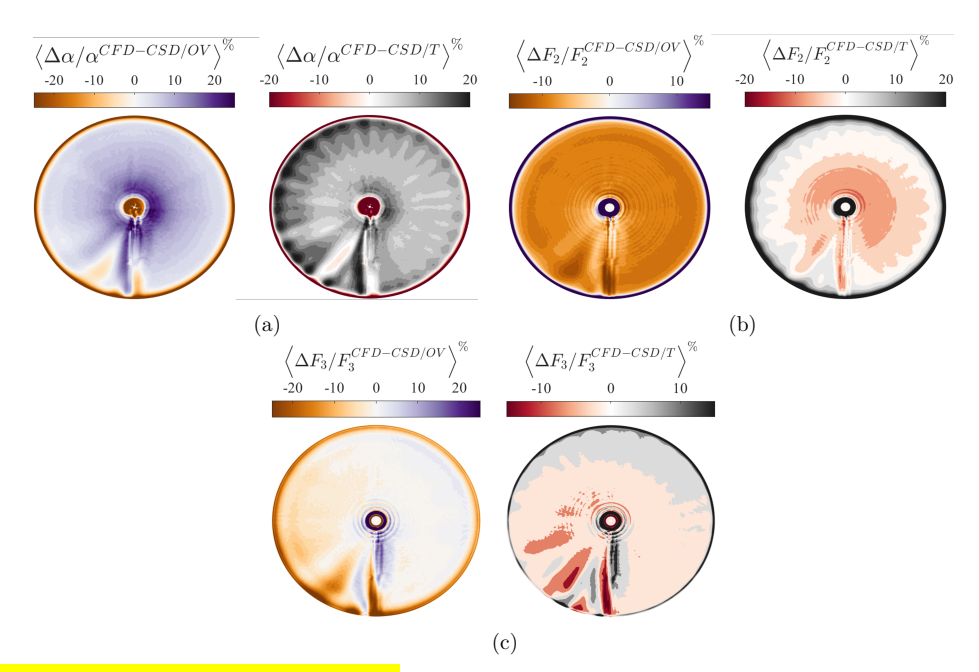


Figure 9: Phase-averaged contour plots of the percentual differences of the aerodynamic quantities between CFD-CSD/C rsus ElastoDyn (left), and CFD-CSD/T versus BeamDyn (right), respectively. (a) Incidence angle, (b) flapwise aerodynamic force, (c) edgewise aerodynamic force.

Notably, similar discrepancies are observed when comparing the CFD-CSD/T solver with the Beam-371 Dyn solvers. However, in this case some high-frequency oscillations are observed for the three aero-372 dynamic quantities. In fact, the same oscillations are observed in the phase averaged quantities at 80% of the blade shown in Figure 8, for both the CFD-CSD/T solver and BeamDyn. Although some 374 mild differences can be observed in their amplitudes and phases, the frequency of these oscillations 375 appears consistent between the two solvers and comparable with the natural frequency of the first 376 torsional mode. Again, this observation indicates that including the torsional degree of freedom in 377 the structural solver is crucial for describing accurately the amplitude and dynamical behaviour of the 378 aerodynamic quantities.

4.3 Power and Thrust coefficients

The aerodynamic loads previously presented are also useful to evaluate the power and thrust coefficients, defined as follows:

$$C_p = \frac{P_d}{\frac{1}{2}\rho A U_\infty^3}, \quad C_t = \frac{T_{aero}}{\frac{1}{2}\rho A U_\infty^2},\tag{9}$$



385

386

387

388 389

390

391

392

393

395

396

397

398

400

401

402

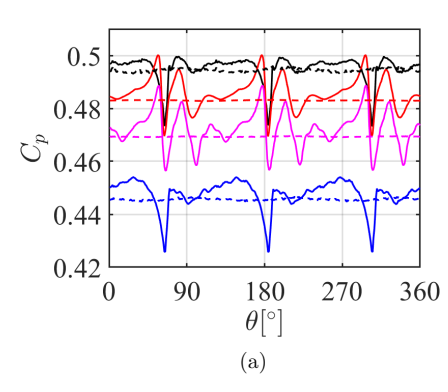
403

404

406

407

408



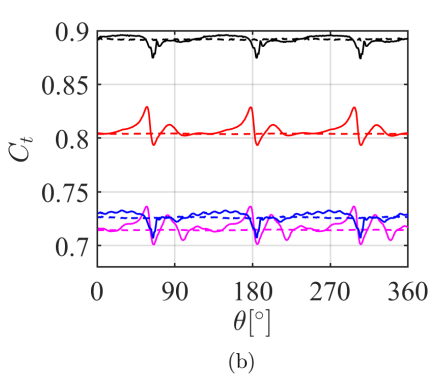


Figure 10: Phase-averaged power (a) and thrust (b) coefficients. CFD-CSD/OV: TN ——, RO ---- CFD-CSD/T: TN ——, RO ---- . ElastoDyn: TN ——, RO ---- . BeamDyn: TN ——, RO ----

where $A = \pi D^2/4$ represents the rotor area, P_d is the aerodynamic power transferred to the rotor and T_{aero} is the overall aerodynamic thrust on the turbine.

Starting from the time history of C_p and C_t , we computed their phase-averaged evolution as reported in Figure 10. The periodic passage of the blades in front of the tower for the TN configuration produces a drop of the curves of about 10%. Eventually, the performance is restored to the value obtained in the RO case through a dynamical behavior consistent with the elastic nature of the structure. The results reflect the dependency of the power and thrust coefficients on the tangential aerodynamic force F_2 and the normal aerodynamic force F_3 at the 80% of the blade, respectively (see Figures 8c and 8b), which are strongly influenced by the presence of the tower. Notice that, also here, we can observe that the drop in the C_p curve appears to be rather consistently predicted by BEM and CFD. The opposite was observed for the NREL 5-MW turbine (Bernardi et al., 2023), where this performance drop is considerably underestimated by the BEM computations. A possible factor that may contribute to this different behaviour may reside in the different relative geometry of the two wind turbines. Indeed, the flow induced by a thinner tower (in diameter units), as in the case of the 15-MW wind turbine, might be better described by a potential flow solution compared to the one induced by a thicker tower, as in the case of the 5-MW wind turbine, and may thus lead to the observed improved agreement between BEM and CFD results. Moreover, the differences in the flow impinging on the blade might also have an effect. In fact, in Bernardi et al. (2023) a uniform inflow was imposed. Whereas, in the present case, due to the shear imposed at the inflow and the limited distance from the ground of the tip of the blade (only $\approx 0.125D$ for the 15MW turbine), the blade is invested by a flow having a much smaller velocity compared to the given value of U_{∞} at hub height, further confirming the increased suitability of a potential flow solution upstream of the tower. Nevertheless, we should recall that this remains a very strong approximation, as also demonstrated by the differences in the forces and angles that have been observed in the previous section (see Figure 9, for instance).

Overall, it can be said that the performance drop due to the passage in front of the tower is somewhat more limited for the 15MW NREL turbine than for the 5MW counterpart, and it is more consistently





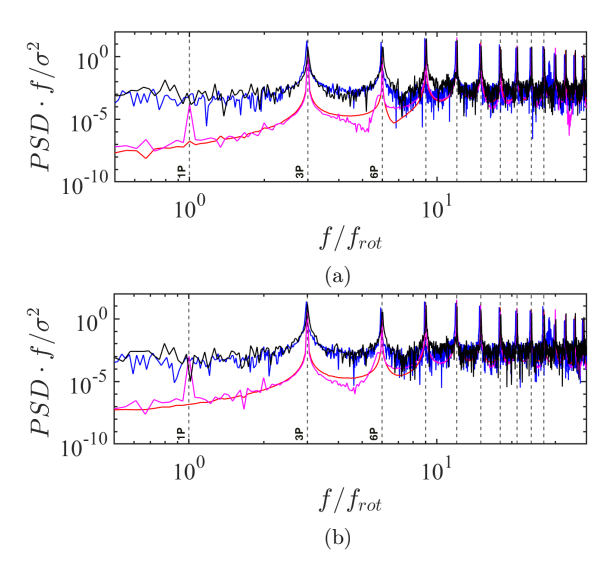


Figure 11: Power Spectral Density (PSD) of the power (a) and thrust (b) coefficients. The vertical dashed lines highlight the rotational frequency of the rotor $P = f_{rot}$ and the multiples of 3P, respectively. CFD-CSD/OV ——, CFD-CSD/T ——, ElastoDyn ——.

predicted by BEM theory and CFD.

Moreover, results seem to suggest that for very large rotors the presence of the tower may constitute a less critical issue for the bla formations than for smaller rotors, although it should yet be taken into account for accurately averabing the turbine's performance oscillations as it still represents a major source of unsteadiness.

The average value of the power coefficient is much larger when the torsional deformation is neglected. This feature is consistently observed by both CFD and BEM approaches. However, one can observe that ElastoDyn underestimates the value of C_p with respect to the corresponding non-torsional CFD model, while the opposite is observed when comparing BeamDyn with the torsional CFD solver. This is most probably due to the fact that BeamDyn predicts higher values of the aerodynamic tangential forces with respect to the CFD-CSD/T approach, which are linked to a smaller torsional deformation as will be shown in figure 12f in the next section.

as will be shown in figure 12f in the next section. Figure 11 shows the premultiplied Power Spectral Density (PSD) of the power (Figure 11a) and thrust (Figure 11b) coefficients evolution. The PSD is normalized by the variance of each coefficient σ^2 and plotted versus the frequency normalized by the rotational frequency of the rotor. f/f_{rot} . In both cases, the CFD-CSD solvers seem to provide a richer representation of the aer mic coefficients, capturing the full range of flow-structure interactions. Indeed, an examination of the low-frequency behavior reveals that both quantities exhibit isolated low-frequency peaks when using the BEM-based solvers, a phenomenon not observed with the CFD-CSD, where the low-frequency range is rather





broadband and does not present particular peaks. It is important to notice that the frequency 1P can be directly linked to the frequency of the passage of the blade in front of the tower, but also to wind shear loads on the blades. Concerning the first point, a potential flow solution as that used in the BEM solver is keen to provide a simple, single-frequency response, whereas a complex, turbulent flow 431 is expected to result in a more broadband spectrum. Concerning the second point, we have to consider 432 that in LES, the power law profile is imposed at the of the domain but it is free to evolve for 433 4 diameters before the wind turbine, altering in a non-trivial way the flow field and the consequent 434 frequency response of the blades. This outcome indicates that the BEM-based solvers tend to overcut the power oscillations associated with low-frequencies that are not exactly equal to 1P or 2P. For all solvers, however, the strongest PSD peaks are to be found at much larger frequencies (3P-6P-9P-12P), 437 as also observed by Pagamonci et al. (2023) by means of URANS aeroelastic simulations of the NREL 438 5-MW, the DTU 10-MW, and the IEA 15-MW turbines. One can also notice that the amplitude 439 associated with the 3P frequency appears to be consistently described by the two solvers, although also in this range the BEM solver appears to overdamp the frequencies in between different peaks. Moreover, a good agreement is evident between the two set of results concerning the value of the 442 frequencies and the level of the PSD for frequencies that are multiples of 3P. 443

4.4 Structural response

444

This section presents the analysis of the structural dynamics. Figure 12 reports the phase-averaged dynamic response of the free extremity of the blade (left column) tion of the entire span (right column). Figure 12a shows how the the time-averaged deformalane deformation is mainly governed by the aerodynamic component of the force normal to the rotor plane and, hence, to the 448 aerodynamic effects, heavily affected by the tower. In fact, it is visible how the tower placed at 449 $\theta = 180^{\circ}$ produces a drop in the deformation, followed by an elastic dynamic response which restores 450 the value far from the pointing-down position. The time-averaged maximum deformation predicted 451 by the CFD-CSD/OV solver is 16% higher compared to the ElastoDyn module and 17% compared to BeamDyn (see Figure 12b). On the other hand, the same quantity predicted by the CFD-CSD/T 453 solver is 17% lower compared to the ElastoDyn module and 13% compared to BeamDyn (see Figure 454 12b). This is consistent with the fact that including the torsional degree of freedom reduces the loads 455 (see figure 8b) and the resulting deformation. Although the trend of deformation with respect to the blade span appears consistent with previous predictions based on URANS (see Pagamonci et al. (2023)), the out-of-plane deformation is rather larger, reaching 16 m at the blade's tip. The amplitude 458 of the deformation is however consis with that obtained by Trigaux et al. (2024) using LES. Figure 459 12c depicts instead the in-plane determation, which is mostly due to gravity. The results show that 460 the shadowing effect of the tower does not influend | squantity. Furthermore, the discrepancies 461 obtained between ElastoDyn and BeamDyn can be a tted to the lack of modes used by the former 462 463 model to describe the translation in the edgewise direction (see Figure 12d). discrepancy does not seem to be linked to the linearity of this model, as the result of the CFD T solver, which 464 is linear as well, is much closer to the BeamDyn results. Moreover, the results of the CFD-CSD/OV 465 and the CFD-CSD/T models are very close to each other. It can be noticed that the amplitude of the 466 oscillation of the in-plane deflection is consistent with that reported by ux et al. (2024), although 467 the sign is opposite due to the different frame of reference used.



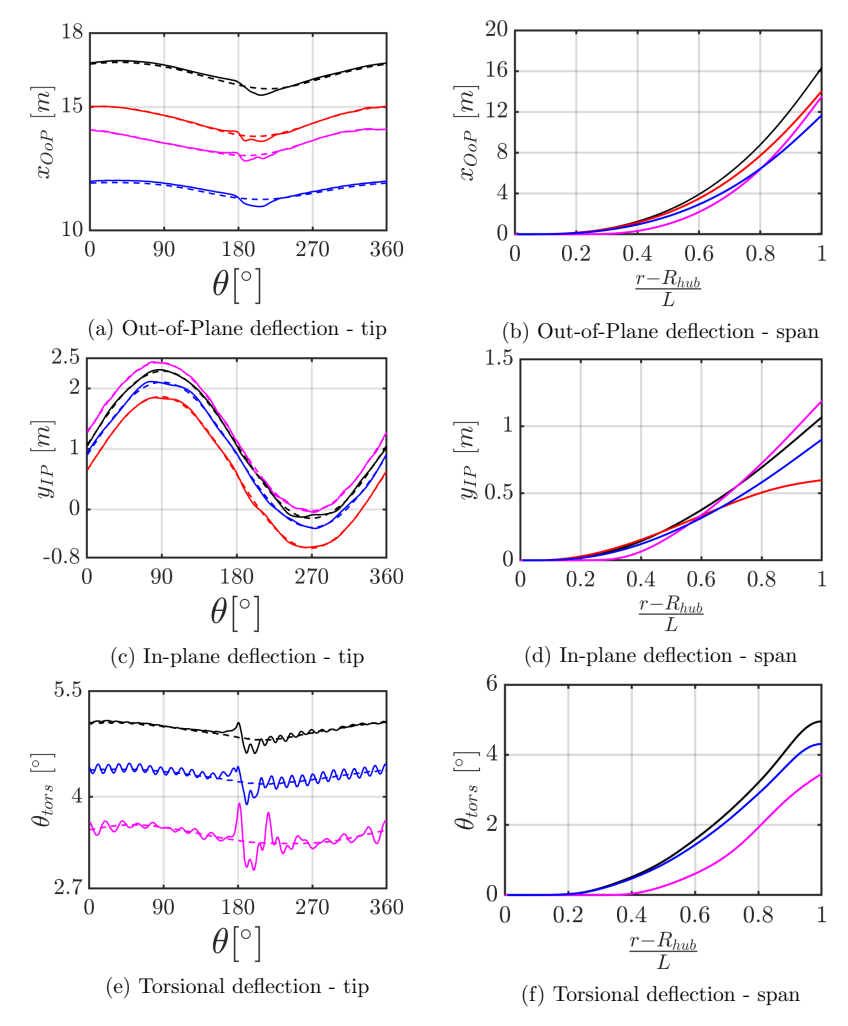


Figure 12: Phase-averaged deflections at the tip of the blade (left column) and time-averaged deflections along the blade span (right column). CFD-CSD/OV: TN ——, RO ----. CFD-CSD/T: TN ——, RO ----. ElastoDyn: TN ——, RO ----. BeamDyn: TN ——, RO ----.

A further significant insight into the deformation phenomenon is provided by the torsional DoF. Figure 12e shows a comparison of the torsional angle at the tip with *BeamDyn*. Significant discrepancies can

be observed between the LES and the BEM approaches, which cannot be reconducted to the different



473

474 475

476

477

478

479

480

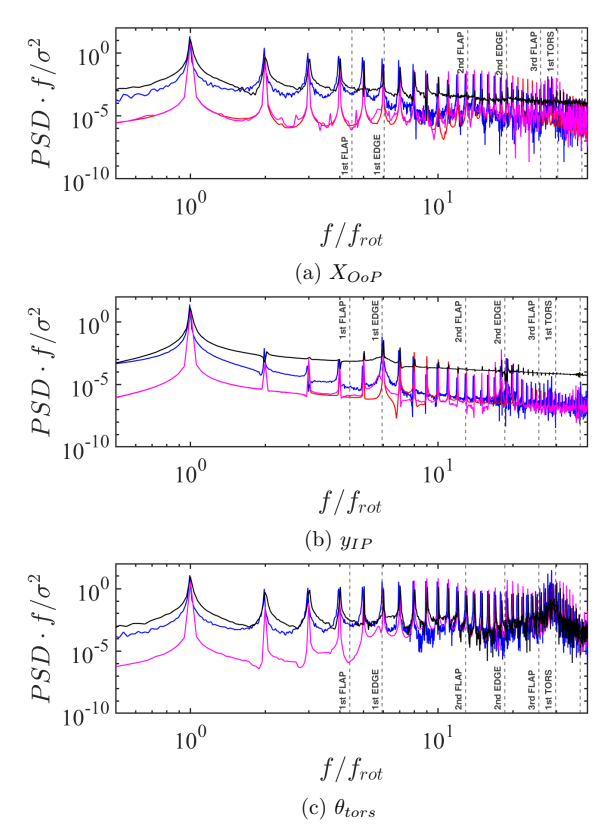


Figure 13: Power Spectral Density (PSD) of the out-of-plane (a), in-plane (b), and torsional (c) deformation of the blade. The vertical dashed lines represent the first 8 eigenfrequencies of the system. CYD-CSD/OV —, CFD-CSD/T — ElastoDyn —, BeamDyn —.

coupling procedures adopted by the models. On the one hand, BeamDyn and CFD-CSD/T both take into account the deformation angle in the coupling (Wang et al., 2016), while in the CFD-CSD/OV solver the angle of attack depends only on the deformation velocity (see Equation 18). However, the gap between the BEM and the CFD-CSD/T curves is quite large. This can be used to the different aerodynamic and structural model used in BEM and LES. The latter is confirmed by the time-averaged torsional deformation along the space ported in Figure 12f where the maximum percentual gap of BeamDyn reaches 29% for the CSD-OCD/OV, and 24% for the CFD-CSD/T. It is noteworthy that the lower torsional deformation resulting from BeamDyn leads to the higher aerodynamic loads observed in figure 8c.

Finally, figure 13 illustrates the Power Spectral Density (PSD) of the blade's tip deformation compo-





nents for the TN configuration (which is characterized by more complex fluid-structure interactions). The premultiplied PSD values are normalized by the variance of the signal, σ^2 , and plotted versus the frequency normalized by the rotor frequency, f/f_{rot} . Spectral results have been corroborated through use of the Welch and Lomb-Scargle PSD estimation algorithms. 485 Figure 13a shows the out-of-plane deformation, which we showed to be influenced mostly by the 486 aerodynamic loading. The results indicate that, for all the numerical approaches used, the observed 487 structural response does not ex a peak corresponding to the first flapwise natural frequency, 488 suggesting that the intrinsic dy so of the structure might play a less prominent role in the deformation process. This is consistent to the results of Trigaux et al. (2024) (see Fire 6 of the cited paper) for the same turbine and similar inflow conditions. However, the second third flapwise 490 491 natural frequencies are indeed recovered by all the numerical models, despite their contribution has a 492 limited energy content. Both the CFD-CSD solvers show larger amplitudes for a broadband range of 493 frequencies than OpenFAST, suggesting that they are more able to capture complex flow interactions, including turbulence-induced vibrations. This effect is particularly pronounced at the lower frequencies, probably due to the large-scale three-dimensional structure of the flow impinging on the turbine, 496 which is not captured by OpenFAST. These aspects seem to be under-represented in the ElastoDyn 497 . Although the ElastoDyn curve aligns with both the CFD-CSD solvers at and BeamDun solu 498 some key frequency veaks, it does not fully account for the fine-scale flow-structure interactions. On 499 the other hand, the BeamDyn curve provides better agreement with the CFD-CSD solvers, especially 500 at higher frequencies near the blade's natural modes, suggesting that BeamDyn captures more of the 501 structural dynamics, particularly the aeroels response. Figure 13b shows the in-plane deforma-502 tion, which is primarily influenced by gravity, centrifugal, and Coriolis forces acting on the blade. The 503 CFD-CSD solvers again demonstrate stronger low-frequency components. 504 Figure 13c presents the torsional deformation for the CFD-CSD/T and BeamDyn solvers, excluding 506 ElastoDyn, which neglects the torsional DoF in the model. Additionally, also this quantity demonstrates that the CFD-CSD curves predict higher amplitudes at low frequencies. However, a good 507 agreement between the two solvers is evident at higher frequencies, especially in the range around the 508 first torsional eigenfrequency. 509

5 Conclusions

510

This study investigated the aeroelastic response of the IEA 15-MW wind turbine by employing a 511 high-fidelity Computational Fluid Dynamics (CFD) solver that couples Large-Eddy Simulation (LES) 513 with a Computational Structural Dynamics (CSD) solver. Two different CSD solvers are considered: the CFD-CSD/OV solver, in which the only structural quantity contributing to the definition of the 514 angle of attack is the deformation velocity, and the CFD-CSD/T solver, in which the instantaneous 515 torsional deformation is also considered when defining the local effective incidence. The results of the 516 two CFD-CSD solvers are compared with those of traditional engineering solvers such as BeamDyn 517 and ElastoDyn, both relying on Blade Element Momentum (BEM) theory. Two case studies were 518 examined: a rotor-only configuration (RO) and one that included the tower and nacelle (TN). 519 In the first instance, a flow analysis uncovered important considerations regarding wake entrainment. 520 In particular, the study found that for the considered turbine, impinged by a laminar sheared inflow,





wake recovery is only slightly hindered by the presence of the tower. The entrainment of kinetic energy driven by the tower leads to higher turbulence levels in the near wake, but then result into a slightly decreased mixing behind the turbine, differently to what has been found for the NREL 5MW wind turbine, whose wake recovery was found to be promoted by the presence of the tower. This finding can have important implications for the aerodynamic loads on downstream turbines in wind farms and overall farm efficiency.

In addition, the Power Spectral Density (PSD) of the power and thrust coefficients revealed that the 528 CFD-CSD solver captures a broader range of flow-structure interactions, with a more broadband low-529 frequency response, compared to the BEM-based solvers. The isolated low-frequency peaks found in 530 BeamDyn and ElastoDyn suggest that these solvers tend to over-simplify the aerodynamic fluctuations 531 associated with phenomena such as wind shear and tower shadowing. For the IEA 15-MW turbine, 532 the performance drop caused by tower passage is less pronounced compared to the data available for 533 smaller turbines such as the NREL 5-MW. The BEM-based solvers show a less pronounced discrepancy with the CFD-CSD predictions, although in this case the resulting oscillations appear overestimated by BEM, while they were underestimated for the 5-MW wind turbine as observed by Bernardi et al. 536 (2023). This may be due to the thinner tower of the 15-MW turbine relative to its rotor diameter, 537 and to the different inflow conditions (sheared in the present case, uniform in previous studies on the 538 5-MW turbine). 539

Concerning the forces on the blade and the incidence angle, one can observe a rather good match between the CFD-CSD/OV solver and *ElastoDyn*, as well as between the CFD-CSD/T model and the *BeamDyn* solver. This is likely due to the presence – or not – of the torsional feedback, while non-linearities of the structural solver appear to have only a limited impact on the observed quantities. In agreement with previous studies, the results thus suggest that including the torsional degree of freedom in the structural solver is crucial for accurately describing the amplitude and dynamical behaviour of the aerodynamic quantities.

Moreover, it is observed that duly taking into account the torsional degree of freedom reduces the value of C_p . This feature is consistently observed by both CFD and BEM approaches. However, one can observe that BeamDyn predicts lower values of the torsional deformation and thus higher values of the aerodynamic tangential forces with respect to the CFD-CSD/T approach, leading to a larger C_p value than that predicted by LES. The CFD-CSD solvers tend to exhibit larger amplitudes at lower frequencies with respect to BEM ones, suggesting a stronger capability to capture complex aerodynamic loading and turbulence effects.

The structural response of the wind turbine blade has been assessed by comparing the out-of-plane, inplane, and torsional deformations obtained from the CFD-CSD solvers, *ElastoDyn*-based, and *Beam-Dyn*-based OpenFAST solver. In-plane deformation, influenced significantly by centrifugal forces, appears to be better captured by the CFD-CSD solvers, especially in the low-frequency range. Concerning the out-of plane deflection, large discrepancies are seen between the two CFD-CSD solvers, as well as between both BEM modules and the LES.

Our results underscore the importance of incorporating torsional deformation effects in the definition of the angle of attack and using high-fidelity aeroelastic models to ensure accurate predictions of wind turbine blade performance with a richer fluid dynamics. Whereas, the linearity of the structural model does not appear to have a strong effect on the aerodynamical quantities, deformations and loads. In



574

575

576

581

582

583

586

587



general, the comparison of the results of the CFD-CSD solver with those of the engineering solver shows differences especially in the region behind the tower. This suggests that the use of a highfidelity CFD approach may be crucial for determining the effect of the tower, the dynamic response of the turbine blades and the wake recovery process. Future work will explore the effect of turbulent fluctuations at the inlet to better investigate the impact

Future work will explore the effect of turbulent fluctuations at the inlet to better investigate the impact of the atmospheric boundary layer on the aerodynamic forces, loads and deformations of the present turbine.

571 A Appendix A. Grid Convergence Study for the LES Simulation

A grid convergence study was conducted to evaluate the sensitivity of the LES results to spatial and temporal resolution. Two simulations were carried out using grids of different densities: a coarse mesh and a finer mesh, with the latter having approximately 40% more grid points than the former in each spatial direction. This allowed for a more detailed resolution of flow structures and aerodynamic quantities. Moreover, the simulation ran with the finer grid uses the same CFL = 0.65 as the coarse grid one. The average time step obtained and the other key parameters of the two LES runs are summarized in Table A1.

Parameter	Coarse Grid	Fine Grid
Total number of cells	5.37×10^{8}	1.36×10^{9}
Largest cell diagonal (m)	5	3.5
Smallest cell diagonal (m)	2.5	1.7
Actuator points per blade	86	128
Average time step (s)	0.024	0.012
Total number of threads	512	768

Table A1: Comparison of the main parameters for the coarse and fine meshes.

The comparison in figure A1 shows that the results obtained using the coarse and fine grids are extremely close each other along the entire blade span. In particular, the curves of the angle of attack are almost indistinguishable, even in the outer portion of the blade, where stronger differences were expected due to tip effects and local three-dimensionality. The maximum deviation of the incidence angle α between the two simulations at 80% of the span reaches a value of $\Delta \alpha_{max} \approx 0.2^{\circ}$, corresponding to a relative difference of 1.6%. Similarly, the aerodynamic force component distributions exhibit negligible variation between the two resolutions, confirming the overall consistency of the LES solution examined in the Sec. 4 with respect to mesh refinement.

These results indicate that the coarse grid accurately captures the main aerodynamic features, making the use of a finer mesh unjustified given its higher computational cost and minimal accuracy gain.



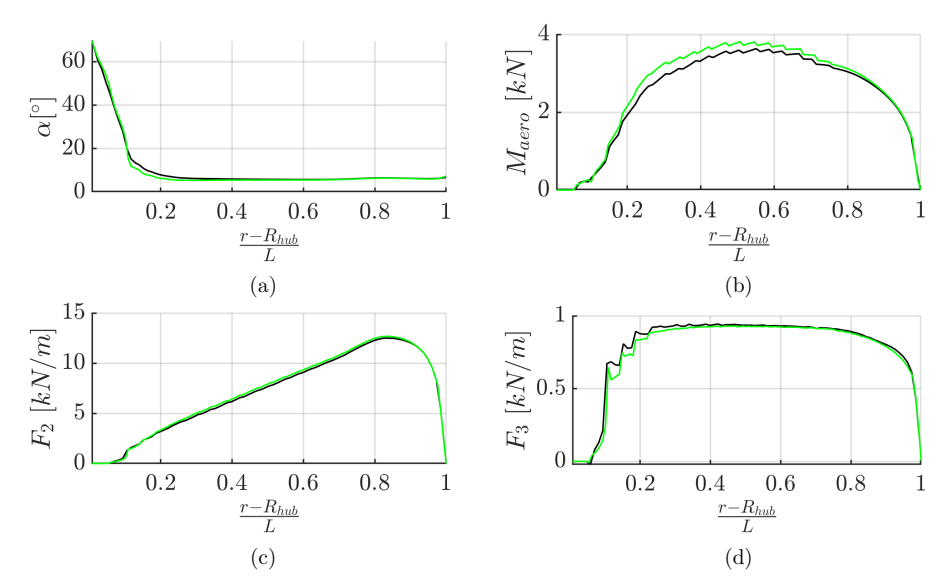


Figure A1: Average aerodynamic quantities along the blade obtained from the coarse grid (black line), and the thick grid (green line). (a) Incidence angle, (b) Aerodynamic pitch moment, (c) flapwise aerodynamic ford edgewise aerodynamic force.

B Appendix B. Validation of the structural model

A preliminary study was conducted to validate the structural model prior to coupling it with the CFD solver. Figure B1 shows the distributions of the structural and constructive properties along the blade, which were utilized as input for the modal CSD analysis. A convergence study to determine the proper number of elements, N_e , (not reported here for brevity) was conducted, leading to the choice $N_e = 80$. Furthermore, the results of the present structural analysis were compared with those of five models including: the prismatic Timoshenko model without torsion (H2-PTNT); the Timoshenko model with a fully populated stiffness matrix (H2-FPM) from the study of Rinker et al. (2020); the 3D Finite Element Analysis (3D FEA) selected from Zhang et al. (2023); the ElastoDyn model; the BeamDyn model. Figure B2 shows the first 8 eigenfrequencies using the present method compared with the results of these models. The computed values of the modal frequencies appear to be consistent with the other results, although some discrepancies in the higher-order modes are observed. Moreover, an analysis of the most important modes was conducted: Table B1 provides the classification of the first 8 modes, whereas, Figures B3, B4, and B5 show the modal displacements for the first spanwise, edgewise, and torsional modes, respectively.



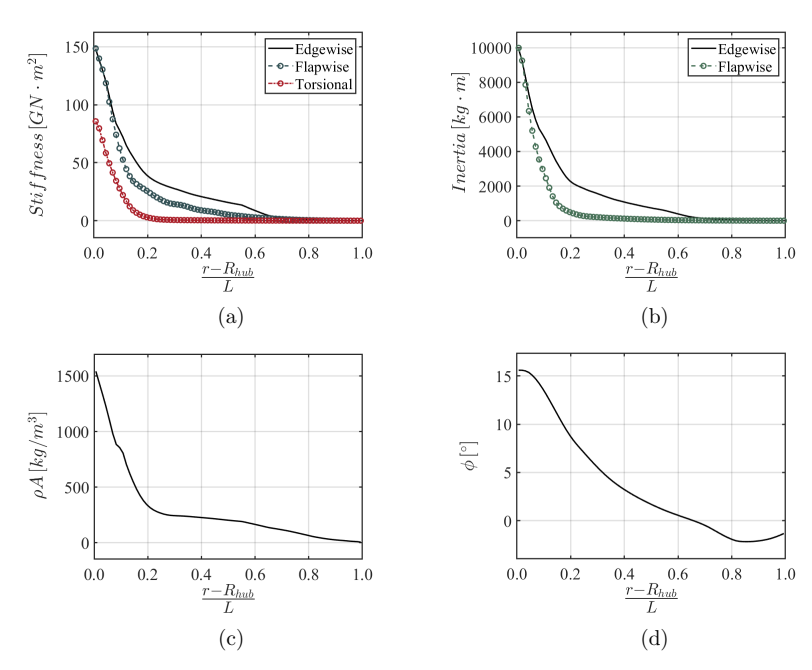


Figure B1: Structural properties of the blade along the span: (a) stiffness, (b) inertia, (c) density, (d) local twist angle.

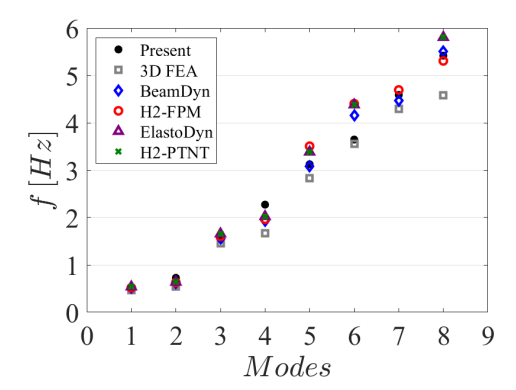


Figure B2: A comparison of the eigenfrequencies computed by different structural models.





#	$f_n[Hz]$	Mode
1	0.5369	1st flapwise
2	0.7267	1st edgewise
3	1.577	2nd flapwise
4	2.267	2nd edgewise
5	3.113	3rd flapwise
6	3.642	1st torsional
7	4.571	3rd edgewise
8	5.385	4th flapwise

Table B1: Classification of the first 8 structural modes.

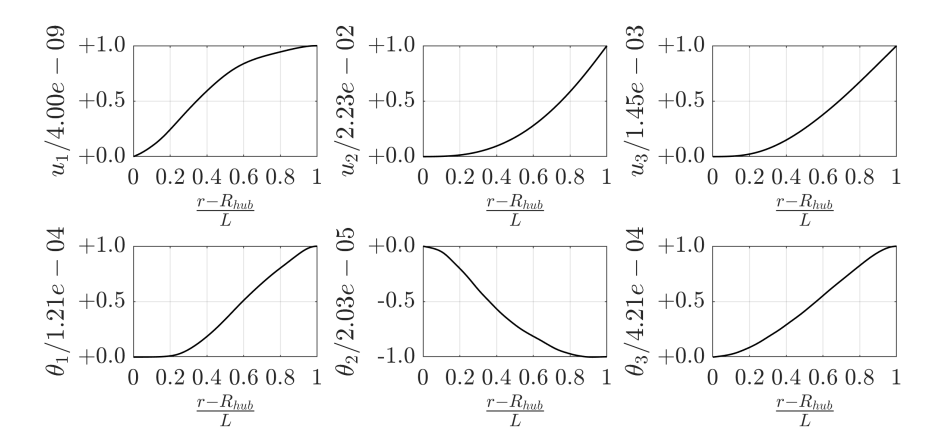


Figure B3: Mode 1 shape for all the DoFs.





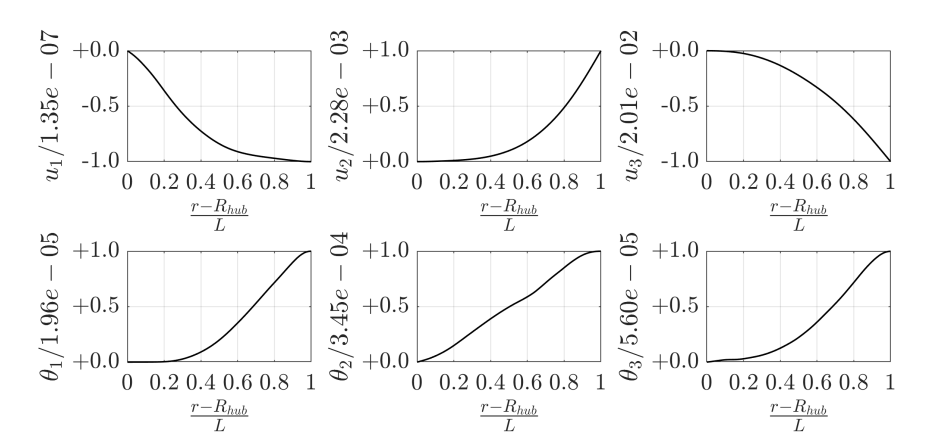


Figure B4: Mode 2 shape for all the DoFs.

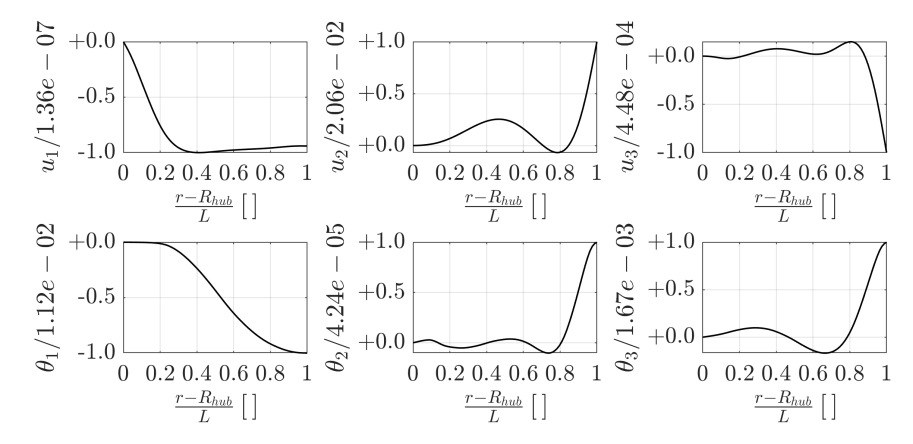


Figure B5: Mode 6 shape for all the DoFs.





- 604 Author contribution. CB: Investigation, Writing Original draft, Formal analysis, Methodology, Soft-
- ware, Validation. SC: Conceptualization, Investigation, Writing Review & Editing, Supervision. FM:
- Methodology, Software, Validation. GDP: Formal analysis, Writing Review & Editing, Methodol-
- 607 ogy, software. SL: Conceptualization, Software, Supervision. PDP: Conceptualization, Investigation,
- 608 Writing Review & Editing, Supervision.
- 609 Competing interests. The authors declare that they have no competing interests.
- 610 Acknowledgments. This study has been partially funded under the National Recovery and Resilience
- 611 Plan (NRRP), Mission 4 Component 2 Investment 1.3 Call for tender No. 1561 of 11.10.2022
- 612 Project code PE0000021, Project title "Network 4 Energy Sustainable Transition NEST", and
- under the PRIN grant 20229YJP33, "Diffuser augmented Wind Turbines for URBban environments"
- 614 (DWTURB). Both are grants of Ministero dell'Università e della Ricerca (MUR), funded by the
- European Union NextGenerationEU. The cooperative work on the 15MW NREL wind turbine
- within the IEA WIND TASK 47 TURBINIA is also acknowledged.

References

- Abdel Hafeez, M. M. and A. A. El-Badawy (2018). Flutter limit investigation for a horizontal axis
 wind turbine blade. *Journal of Vibration and Acoustics* 140(4), 041014.
- Bayati, I., M. Belloli, L. Bernini, and A. Zasso (2017). Aerodynamic design methodology for wind
 tunnel tests of wind turbine rotors. Journal of Wind Engineering and Industrial Aerodynamics 167,
 217–227.
- Bazilevs, Y., M.-C. Hsu, J. Kiendl, R. Wüchner, and K.-U. Bletzinger (2011). 3d simulation of wind
 turbine rotors at full scale. part ii: Fluid-structure interaction modeling with composite blades.
 International Journal for Numerical Methods in Fluids 65 (1-3), 236 253. Cited by: 441.
- Bernardi, C., G. D. Posta, P. D. Palma, S. Leonardi, F. Bernardoni, M. Bernardini, and S. Cherubini
 (2023, may). The effect of the tower's modeling on the aero-elastic response of the nrel 5 mw wind
 turbine. Journal of Physics: Conference Series 2505(1), 012037.
- Burton, T., N. Jenkins, D. Sharpe, and E. Bossanyi (2011). Wind energy handbook. John Wiley &
 Sons.
- Chen, X. (2017). Experimental investigation on structural collapse of a large composite wind turbine
 blade under combined bending and torsion. Composite Structures 160, 435–445.
- Chung, J. and G. Hulbert (1993). A time integration algorithm for structural dynamics with improved
 numerical dissipation: the generalized-α method.





- Courant, R., K. Friedrichs, and H. Lewy (1967). On the partial difference equations of mathematical
 physics. *IBM journal of Research and Development 11*(2), 215–234.
- Damgaard, M., L. B. Ibsen, L. V. Andersen, and J. K. Andersen (2013). Cross-wind modal properties
 of offshore wind turbines identified by full scale testing. *Journal of Wind Engineering and Industrial* Aerodynamics 116, 94–108.
- Damiani, R., J. Jonkman, and G. Hayman (2015). Subdyn user's guide and theory manual. Technical report, National Renewable Energy Lab.(NREL), Golden, CO (United States).
- De Cillis, G., O. Semeraro, S. Leonardi, P. De Palma, and S. Cherubini (2022). Dynamic-modedecomposition of the wake of the nrel-5mw wind turbine impinged by a laminar inflow. *Renewable Energy* 199, 1–10.
- Della Posta, G., S. Leonardi, and M. Bernardini (2022). A two-way coupling method for the study of
 aeroelastic effects in large wind turbines. Renewable Energy 190, 971–992.
- Della Posta, G., S. Leonardi, and M. Bernardini (2023). Large eddy simulations of a utility-scale horizontal axis wind turbine including unsteady aerodynamics and fluid-structure interaction modelling.
 Wind Energy 26(1), 98–125.
- Dong, X., J. Lian, H. Wang, T. Yu, and Y. Zhao (2018). Structural vibration monitoring and operational modal analysis of offshore wind turbine structure. Ocean Engineering 150, 280–297.
- Gaertner, E., J. Rinker, L. Sethuraman, F. Zahle, B. Anderson, G. Barter, N. Abbas, F. Meng,
 P. Bortolotti, W. Skrzypinski, et al. (2020). Definition of the iea 15-megawatt offshore reference
 wind turbine.
- Gaertner, E., J. Rinker, L. Sethuraman, F. Zahle, B. Anderson, G. Barter, N. Abbas, F. Meng,
 P. Bortolotti, W. Skrzypinski, G. Scott, R. Feil, H. Bredmose, K. Dykes, M. Sheilds, C. Allen, and
 A. Viselli (2020). Definition of the IEA 15-megawatt offshore reference wind turbine. Technical
 report, International Energy Agency.
- 659 Hansen, M. (2015). Aerodynamics of wind turbines. Routledge.
- Hansen, M. H. (2007). Aeroelastic instability problems for wind turbines. Wind Energy: An International Journal for Progress and Applications in Wind Power Conversion Technology 10(6),
 551-577.
- 663 Jonkman, J. The New Modularization Framework for the FAST Wind Turbine CAE Tool.
- Jonkman, J. M., G. Hayman, B. Jonkman, R. Damiani, and R. Murray (2015). Aerodyn v15 user's
 guide and theory manual. NREL Draft Report 46.
- Manwell, J. F., J. G. McGowan, and A. L. Rogers (2010). Wind energy explained: theory, design and
 application. John Wiley & Sons.





- Martinez-Tossas, L. A., M. J. Churchfield, A. E. Yilmaz, H. Sarlak, P. L. Johnson, J. N. Sørensen,
- J. Meyers, and C. Meneveau (2018). Comparison of four large-eddy simulation research codes and
- effects of model coefficient and inflow turbulence in actuator-line-based wind turbine modeling. 670
- Journal of Renewable and Sustainable Energy 10(3). 671
- Moeller, T. (1997). Blade cracks signal new stress problem. WindPower Monthly 25. 672
- Moriarty, P. J. and A. C. Hansen (2005, 1). Aerodyn theory manual. 673
- Orlandi, P. (2012). Fluid flow phenomena: a numerical toolkit, Volume 55. Springer Science & Business Media. 675
- Orlandi, P. and S. Leonardi (2006). Dns of turbulent channel flows with two-and three-dimensional 676 roughness. Journal of Turbulence (7), N73. 677
- Pagamonci, L., F. Papi, F. Balduzzi, S. Xie, J. Sadique, P. Scienza, and A. Bianchini (2023). To what 678 extent is aeroelasticity impacting multi-megawatt wind turbine upscaling? a critical assessment. In 679 Journal of Physics: Conference Series, Volume 2648, pp. 012005. IOP Publishing. 680
- Pino Martín, M., U. Piomelli, and G. V. Candler (2000). Subgrid-scale models for compressible 681 large-eddy simulations. Theoretical and Computational Fluid Dynamics 13, 361–376. 682
- Reschke, C. (2005). Flight loads analysis with inertially coupled equations of motion. In AIAA 683 Atmospheric Flight Mechanics Conference and Exhibit, pp. 6026.
- Rinker, J., E. Gaertner, F. Zahle, W. Skrzypiński, N. Abbas, H. Bredmose, G. Barter, and K. Dykes 685 (2020). Comparison of loads from hawc2 and openfast for the lea wind 15 mw reference wind turbine. 686 In Journal of Physics: Conference Series, Volume 1618, pp. 052052. IOP Publishing. 687
- Sabale, A. K. and N. K. V. Gopal (2019). Nonlinear aeroelastic analysis of large wind turbines under 688 turbulent wind conditions. AIAA Journal 57(10), 4416-4432. 689
- Saltari, F., C. Riso, G. D. Matteis, and F. Mastroddi (2017). Finite-element-based modeling for flight 690 dynamics and aeroelasticity of flexible aircraft. Journal of Aircraft 54(6), 2350–2366. 691
- Santoni, C., K. Carrasquillo, I. Arenas-Navarro, and S. Leonardi (2017). Effect of tower and nacelle 692 on the flow past a wind turbine. Wind Energy 20(12), 1927–1939. 693
- Santoni, C., E. J. García-Cartagena, U. Ciri, L. Zhan, G. Valerio Iungo, and S. Leonardi (2020). One-694 way mesoscale-microscale coupling for simulating a wind farm in north texas: Assessment against scada and lidar data. Wind Energy 23(3), 691–710.
- Schepers, J., K. Boorsma, H. Madsen, G. Pirrung, G. Bangga, G. Guma, T. Lutz, T. Potentier, C. Braud, E. Guilmineau, A. Croce, S. Cacciola, A. P. Schaffarczyk, B. A. Lobo, S. Ivanell, H. As-698 muth, F. Bertagnolio, N. Sørensen, W. Z. Shen, C. Grinderslev, A. M. Forsting, F. Blondel, P. Bozon-699
- net, R. Boisard, K. Yassin, L. Hoening, B. Stoevesandt, M. Imiela, L. Greco, C. Testa, F. Magionesi, 700
- G. Vijayakumar, S. Ananthan, M. A. Sprague, E. Branlard, J. Jonkman, M. Carrion, S. Parkinson, 701





- and E. Cicirello (2021, May). IEA Wind TCP Task 29, Phase IV: Detailed Aerodynamics of Wind
 Turbines.
- Shen, W. Z., R. Mikkelsen, J. N. Sørensen, and C. Bak (2005). Tip loss corrections for wind turbine
 computations. Wind Energy: An International Journal for Progress and Applications in Wind
 Power Conversion Technology 8(4), 457–475.
- Sørensen, J. N. (2011). Aerodynamic aspects of wind energy conversion. Annual Review of Fluid
 Mechanics 43(1), 427–448.
- Trigaux, F., P. Chatelain, and G. Winckelmans (2024). Investigation of blade flexibility effects on the loads and wake of a 15 mw wind turbine using a flexible actuator line method. Wind Energy Science 9(8), 1765–1789.
- Troldborg, N. (2009). Actuator line modeling of wind turbine wakes. Ph. D. thesis, Technical University
 of Denmark.
- Vermeer, L., J. N. Sørensen, and A. Crespo (2003). Wind turbine wake aerodynamics. *Progress in aerospace sciences* 39(6-7), 467–510.
- Wang, L., X. Liu, and A. Kolios (2016). State of the art in the aeroelasticity of wind turbine blades:
 Aeroelastic modelling. Renewable and Sustainable Energy Reviews 64, 195–210.
- Wang, Q., J. Jonkman, M. Sprague, and B. Jonkman (2016). Beamdyn user's guide and theory
 manual. National Renewable Energy Laboratory.
- Yu, D. O. and O. J. Kwon (2014). Predicting wind turbine blade loads and aeroelastic response using
 a coupled cfd-csd method. Renewable Energy 70, 184 196. Cited by: 111.
- Zahle, F., A. Barlas, K. Lønbæk, P. Bortolotti, D. Zalkind, L. Wang, C. Labuschagne, L. Sethuraman,
 and G. Barter (2024). Definition of the IEA Wind 22-Megawatt Offshore Reference Wind Turbine.
 Technical University of Denmark. DTU Wind Energy Report E-0243 IEA Wind TCP Task 55.
- Zhang, Y., Y. Song, C. Shen, and N.-Z. Chen (2023). Aerodynamic and structural analysis for blades
 of a 15mw floating offshore wind turbine. Ocean Engineering 287, 115785.
- Zheng, J., N. Wang, D. Wan, and S. Strijhak (2023). Numerical investigations of coupled aeroelastic
 performance of wind turbines by elastic actuator line model. Applied Energy 330, 120361.